

Subsidence associated with the LUSI mud eruption, East Java, investigated by SAR interferometry

Yo Fukushima^{a,b,*}, Jim Mori^a, Manabu Hashimoto^a, Yasuyuki Kano^a

^a Disaster Prevention Research Institute, Kyoto University, Gokasho, Uji 611-0011, Japan

^b Department of Geophysics, Stanford University, 397 Panama Mall, Stanford, CA, USA

ARTICLE INFO

Article history:

Received 30 April 2008

Received in revised form

30 January 2009

Accepted 2 February 2009

Available online 11 February 2009

Keywords:

SAR interferometry

Boundary element method

Mud volcano

LUSI

East Java

PALSAR

ALOS

ABSTRACT

A mud volcano LUSI initiated its eruption on 29 May 2006, adjacent to a hydrocarbon exploration well in East Java. Ground subsidence in the vicinity of the LUSI eruptive vent was well recorded by a Synthetic Aperture Radar (SAR) PALSAR onboard the Japanese ALOS satellite. We apply an Interferometric SAR (InSAR) technique on ten PALSAR data scenes, acquired between 19 May 2006 and 21 May 2007, in order to obtain continuous maps of ground displacements around LUSI. Although the displacements in the area closest to the eruptive vent (spatial extension of about 1.5 km) are not detectable because of the erupted mud, all the processed interferograms indicate subsidence in an ellipsoidal area of approximately 4 km (north–south) \times 3 km (east–west), centered at the main eruptive vent. In particular, interferograms spanning the first four months until 4 Oct. 2006 and the subsequent 46 days between 4 Oct. 2006 and 19 Nov. 2006 show at least about 70 cm and 80 cm of displacements away from the satellite, respectively. Possible causes of the subsidence, i.e., 1) loading effect of the erupted mud, 2) creation of a cylindrical mud conduit, and 3) pressure decrease and depletion of materials at depth, are investigated. The effects of the first two causes are found to be insufficient to explain the total amount of subsidence observed in the first six months. The third possibility is quantitatively examined using a boundary element approach by modeling the source of deformation as a deflating oblate spheroid. The spheroid is estimated to lie at depths of a few hundred to a thousand meters. The estimated depths are significantly shallower than determined from analyses of erupted mud samples; the difference is explained by presence of significant amount of inelastic deformation including compaction and downward transfer of material.

© 2009 Elsevier Ltd. All rights reserved.

1. Introduction

On 29 May 2006, an eruption of mud, fluid and steam started in the Porong area of Sidoarjo, East Java (Fig. 1), adjacent to a 2833 m deep hydrocarbon exploration well called Banjarpanji-1. This eruption was later named LUSI, for Lumpur (mud) Sidoarjo (van Noorden, 2006). The eruption initiated two days after an Mw 6.3 earthquake that occurred approximately 250 km southwest of the eruption site near the city of Yogyakarta. There is an ongoing debate whether or not the earthquake triggered the mud eruption (Manga, 2007; Davies et al., 2007, 2008; Mazzini et al., 2007). As of October 2008, the area covered by the mud flows is 6.7 km² (A. Mazzini, personal communication, 2008). As of May 2007, approximately 30 000 people have been displaced despite the continuous construction of dikes around the eruption site to contain the mud

(Mazzini et al., 2007). At the time of this writing (December 2008), the eruption is still continuing.

The eruption has been well recorded by a synthetic aperture radar (SAR) named PALSAR (Phased-Array L-band SAR) onboard the Japanese Earth observation satellite ALOS. One of the principal purposes of PALSAR is Interferometric SAR (InSAR), a technique to map ground displacements with high spatial resolution (several to tens of meters) at centimeter-level precision (e.g. Massonnet and Feigl, 1998; Hanssen, 2001). PALSAR uses an L-band wavelength (23.6 cm), while many other space-borne SAR sensors use shorter wavelengths of the C-band and X-band. It has been shown that the L-band has a great advantage over the C-band and X-band for detecting ground displacement signals on vegetated areas (e.g. Rosen et al., 1996). The eruption site is surrounded by paddy fields, for which the L-band advantage is effective.

In this study, a set of PALSAR interferograms, spanning different time periods, are computed to measure subsidence associated with the LUSI mud eruption. InSAR has been useful for studying land subsidence associated with ground water movements (e.g. Amelung et al., 1999; Gournelen et al., 2007), mining (e.g. Carnec and

* Corresponding author. Disaster Prevention Research Institute, Kyoto University, Gokasho, Uji, 611-0011, Japan. Tel.: +81 774 38 4196; fax: +81 774 38 4190.

E-mail address: yofukushima@rcep.dpri.kyoto-u.ac.jp (Y. Fukushima).

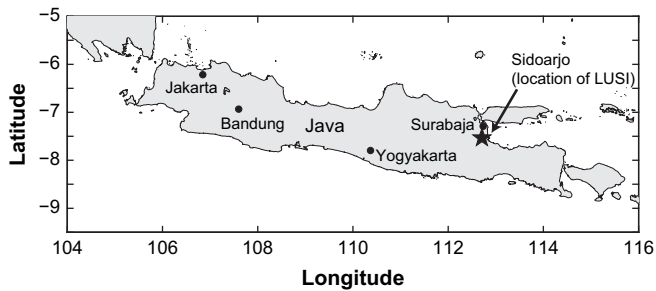


Fig. 1. Map of Java showing the location of the mud volcano LUSI.

Delacourt, 2000; Deguchi et al., 2007a), and geothermal and oil exploitation (e.g. Massonnet et al., 1997; Fielding et al., 1998). The computed interferograms are interpreted using an inversion method that combines a boundary element method with a Monte-Carlo inversion algorithm (Fukushima et al., 2005). The goal of this work is to evaluate possible subsidence mechanisms. Deguchi et al. (2007b) and Abidin et al. (2008) also performed similar InSAR analyses using PALSAR data, but their study was concentrated on the measurements of the ground subsidence and not on the interpretation.

2. PALSAR interferograms

2.1. Data processing

InSAR uses two SAR images to measure displacements in the radar's look (line-of-sight; LOS) direction that occurred between the times of acquisition. ALOS orbit parameters allow views of the same place on Earth from the same point in space every 46 days. The PALSAR instrument can acquire images in different off-nadir angles between 9.9° and 50.8°. Images acquired at the same orbital location at the same off-nadir angle (or same incidence angle) cover approximately the same ground area, and can be used in InSAR processing.

Table 1 summarizes the processed SAR interferograms covering the eruption site. Theoretical studies show that the coherence of InSAR signals is inversely proportional to the perpendicular baseline (a component of the distance between the satellite positions of two acquisitions, perpendicular to the LOS direction) (Zebker and Villasenor, 1992). The interferometric pairs in Table 1 were selected in such a way that the ground deformation is monitored without any missing time intervals, while avoiding (if possible) use of large perpendicular baseline pairs. The largest perpendicular baseline was about 2 km, in which case we could still obtain signals associated with the LUSI activity, as we will see in the next subsection.

Table 1

PALSAR interferograms processed in this study. A1–A4: (path, frame) = (430, 7020). A5: (path, frame) = (427, 7030). D1–D3: (path, frame) = (89, 3780).

ID ^a	Incidence Angle (°)	Dates (yy.mm.dd)	Perpendicular baseline (m)
A1	48.6	06.05.19–06.10.04	2067
A2	48.6	06.10.04–06.11.19	458
A3	48.6	06.11.19–06.02.19	–1153
A4	48.6	06.01.04–07.02.19	1416
A5	39.6	06.12.30–07.02.14	1353
D1	37.7	07.01.03–07.02.18	1663
D2	37.7	07.02.18–04.04.05	106
D3	37.7	07.04.05–07.05.21	–434

^a A and D stand for ascending and descending orbits, respectively.

As the radar is looking roughly from a west-vertical direction for ascending orbits (satellite traveling south to north) and from a east-vertical direction for descending orbits (north to south), interferograms from both ascending and descending orbits allow us to constrain the direction of displacements.

Interferograms were computed from PALSAR level 1.0 products (raw data) using the GAMMA software. Processing was done on whole image scenes of approximately 80 km × 80 km. For subtracting topographic fringes and geocoding, a digital elevation model (DEM) obtained from the Shuttle Radar Topography Mission (SRTM; Farr and Kobrick, 2000) was used. A typical error in SRTM DEMs is less than 10 m (Berry et al., 2007), which results in negligible phase error due to topography, even for the interferogram with the longest baselines. Interferograms were adaptively filtered in the frequency domain to enhance the signal-to-noise ratio (Goldstein and Werner, 1998). No corrections for atmospheric phase delays were applied, meaning that artifacts equivalent to several centimeters of LOS displacements might appear if atmospheric conditions at the times of two acquisitions were different. Orbit inaccuracy leads to ramp-type residual fringes; these fringes were removed by assuming two-dimensional quadratic phase functions. It should be noted that any quadratic signals due to real deformation, if any, were undesirably removed as well by this treatment.

2.2. Processed interferograms

Fig. 2 shows full-scene SAR interferograms listed in Table 1 superimposed on SAR intensity images. Topography-correlated signals observed on mountains in the southern part of the interferograms are most likely due to atmospheric phase delays. Across a few tens of kilometers around the eruption site, signals equivalent to a few centimeters of LOS displacements (color change from cyan to magenta) are observed in some interferograms. Because there is no consistency in the shape or presence of the signals, they are probably also due to atmospheric noise and are not treated further in this paper.

Closer look into the LUSI eruption site shows a significant deformation signal (Figs. 3 and 4). All interferograms are characterized by signals consistent with subsidence around the eruptive vent (zone A in Fig. 4). The interferograms A1–A3 also show a signal consistent with subsidence a few kilometers northeast of the eruptive vent (zone C in Fig. 4). Deguchi et al. (2007b) attribute the cause of this anomaly to another natural gas production well existing in this area. We assume that this signal is not directly related to the LUSI activity. East of the main subsidence area of zone A, approximately 12 cm and 5 cm of displacements toward the satellite are observed (zone B in Fig. 4) in the interferograms A1 and A2, respectively. These signals in zone B can be explained by a deflating deformation source lying under the main subsidence area (see Section 3). There was evidence of faulting from displaced rail tracks to the west of the mud-covered area in September 2006 (Media Center LUSI, 2006; Mazzini et al., 2007). Probably because the location of the displaced rail tracks is very close to the border of the mud-covered area, the displacements associated with this faulting cannot be recognized in the interferogram A1. Outside of the main subsidence area, no clear discontinuity in the fringe pattern is discernible, indicating that there was no near-surface faulting of more than a few centimeters over a spatial extent of more than tens of meters during the observation time interval.

Range increase toward the location of the eruptive vent is observed both from ascending and descending directions throughout the observation period (Fig. 3), indicating that the dominant sense of deformation is downward (subsidence). Interferograms A1 and A2 show up to 6–7 ellipsoidal fringes centered on the eruptive vent, corresponding to about 70 cm and 80 cm of

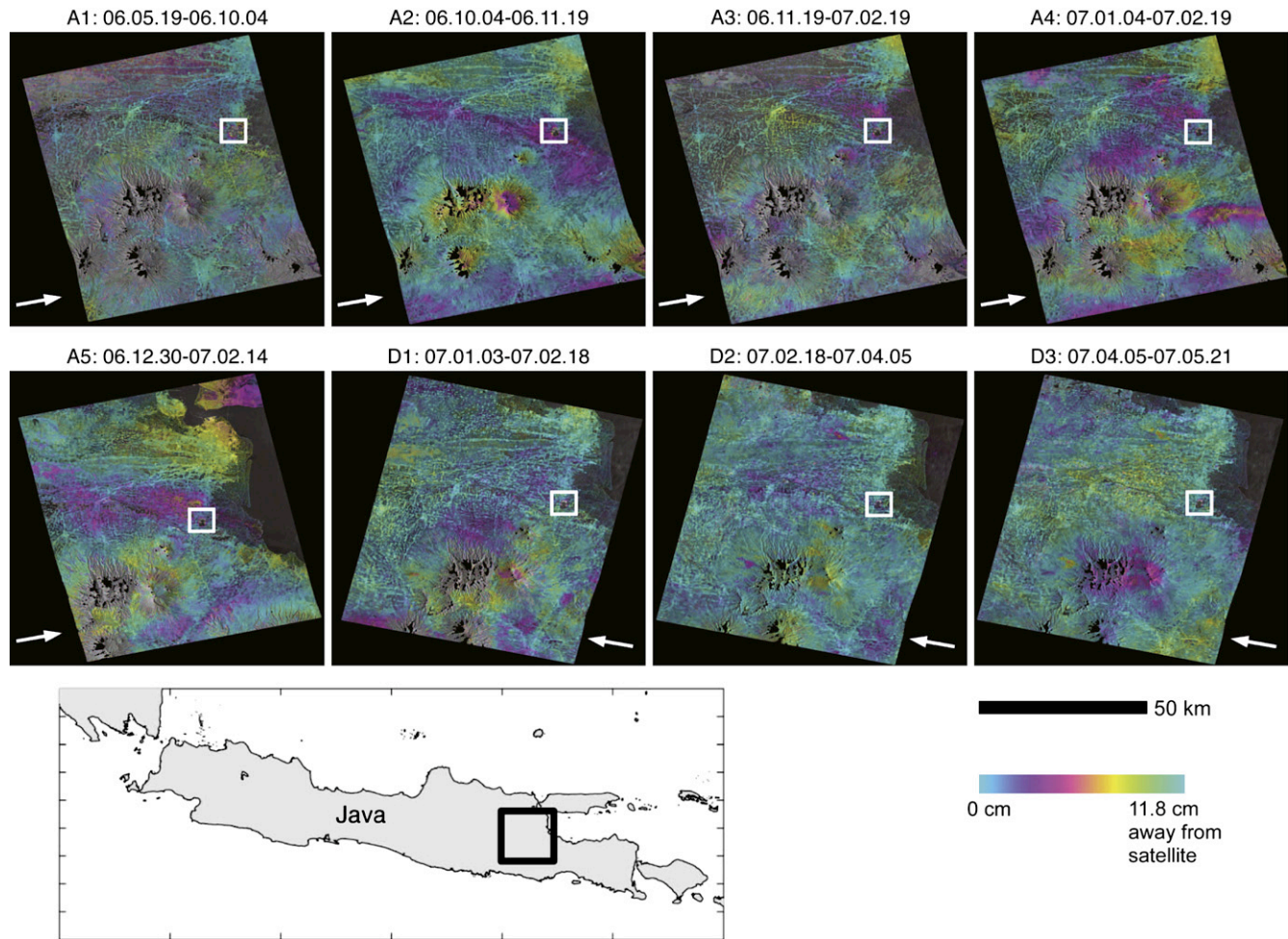


Fig. 2. Full-scene SAR interferograms processed in this study, superimposed on SAR intensity images. Colors correspond to phase values from 0 to 2π , with one cycle change equivalent to 11.8 cm of LOS (line-of-sight) displacements. Color changes from cyan \rightarrow magenta \rightarrow yellow indicates the ground is moving away from the satellite. Arrows show the ground projection of the LOS direction. White squares denote the area coverage of the magnified interferograms of LUSI shown in Fig. 3. Black square in the map shows the approximate location of the full-scene interferograms (For interpretation of the references to color in this figure legend, the reader is referred to the web version of this article.).

ground displacement away from the satellite. These results indicate about 150 cm of LOS displacements in the first 174 days of the eruption. Considering the inclined LOS direction, the vertical component of the deformation field is probably much higher. Because InSAR assumes that the scattering characteristics on the ground target do not differ at the times of acquisition, no signal could be obtained where erupted mud covered the ground surface between SAR acquisitions. Our detected amount of maximum displacement is therefore a minimum estimate. In effect, GPS data at points closer to the eruptive vent indicate subsidence of several meters (Mazzini et al., 2007; Abidin et al., 2008; Istadi et al., 2009). Although GPS data cannot be directly compared with InSAR data because of different time intervals and/or different data location, no obvious inconsistency is found between the two datasets.

After 19 Nov. 2006, the interferograms indicate one or two fringes around the northern rim of the mud-covered area (Fig. 3). The phase changes are all consistent with subsidence. No clear fringes inside the visible ellipsoidal fringes can be identified, even for non-flooded areas, preventing estimation of the total amount of subsidence from the interferograms. The non-visibility of fringes is probably due to disturbance of the ground surface by isolated seepages around the mud-covered area (Mazzini et al., 2007) and/or inelastic deformation associated with fracturing. In the following

section, the interferograms A1 and A2, which contain more coherent signals than the rest, are quantitatively analyzed.

3. Modeling

3.1. Possible subsidence mechanisms

Possible driving sources of subsidence include: (a) loading by the weight of the erupted mud, (b) shrinking of the circular mud conduit due to horizontal compression, and (c) volume loss at depths caused by release of pore overpressure and depletion of material (Fig. 5).

The total amount of erupted mud was estimated to be $2.7 \times 10^7 \text{ m}^3$ as of March 2007 (Mazzini et al., 2007) and $3.7 \times 10^7 \text{ m}^3$ as of May 2007 (Istadi et al., submitted for publication). Loading by the weight of the mud causes ground subsidence, which is known as the Boussinesq problem (Fig. 5(a)). If a point vertical loading F is applied at the origin of the half-space $z \geq 0$, the resulting displacements at the surface $z = 0$ are (Jaeger et al., 2007)

$$u_x = \frac{(1 + \sigma)(1 - 2\sigma)F}{2\pi E} \frac{x}{R^2}, \quad (1)$$

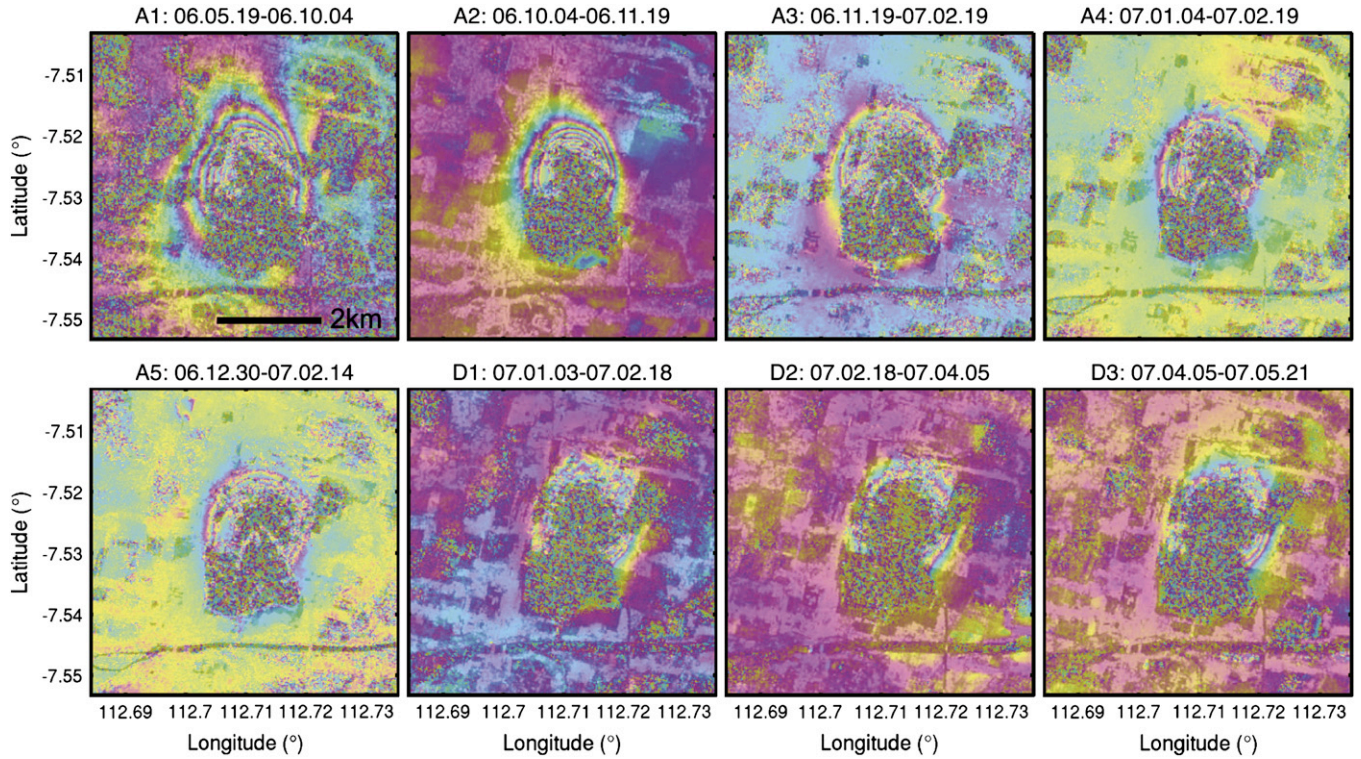


Fig. 3. Magnified images of the SAR interferograms shown in Fig. 2. The back-scatter energy of the SAR microwave on the mud-covered area is small and homogeneous, which allows us to distinguish the extent of the flooded area from the intensity.

$$u_y = \frac{(1 + \sigma)(1 - 2\sigma)F}{2\pi E} \frac{y}{R^2}, \quad (2)$$

$$u_z = -\frac{(1 - \sigma^2)F}{2\pi E} \frac{1}{R}, \quad (3)$$

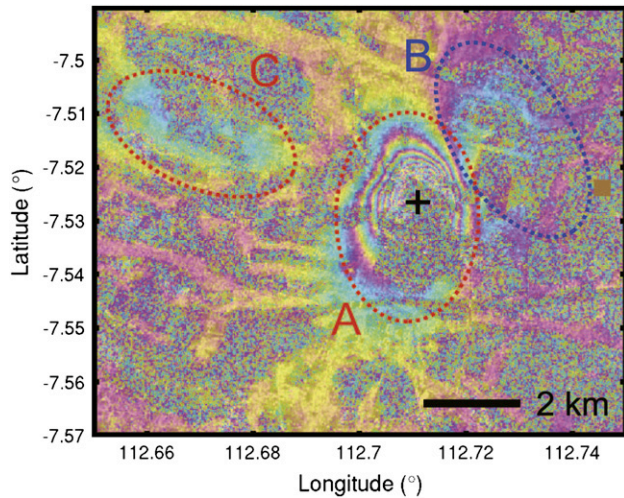


Fig. 4. Magnified image of the interferogram A1 (upper left image of Fig. 2). Red and blue circles are areas where range increases and decreases are observed, respectively, where range refers to the distance between the satellite and the ground. Plus sign denotes the location of the main eruptive vent. (a). Range increase in an ellipsoidal area centered at the eruptive vent. (b). Range decrease, also visible in the interferogram A2. (c). Range increase also observed in the other interferograms. The cause of this anomaly will not be further investigated in this study (For interpretation of the references to color in this figure legend, the reader is referred to the web version of this article.).

where R is the distance from the origin to the point $(x, y, 0)$, E and σ are Young's modulus and Poisson's ratio, respectively.

The well log data at Banjarpanji-1 well and nearby Wunut-4 well suggest Young's modulus of about 1 GPa for depths smaller than 1800 m (unpublished data of Lapindo). Considering that the static Young's modulus can be as low as a fraction of the dynamic Young's modulus for highly porous media (Cheng and Johnston, 1981; van Heerden, 1987), $E = 0.1$ GPa is assumed here. Poisson's ratio σ affects the deformation amplitudes less and is assumed to be 0.25. The point loading F can be approximated by $\rho g V$, where ρ and V are the density and volume of the mud, respectively, and g is the gravity acceleration which equals to 9.8 m/s^2 . Water and sediment contents of the mud erupted at the beginning of the eruption were reported between 60 and 70% and 40 and 30%, respectively (Mazzini et al., 2007; Istadi et al., submitted for publication). To be conservative, the ratio of water and sediment contents is assumed to be 60:40. Further considering the average density of the sediment 2100 kg/m^3 (derived from unpublished well log data of Lapindo) makes the mud density to be 1440 kg/m^3 . The mud volume V is estimated to be $7.3 \times 10^6 \text{ m}^3$ for the first five months from the flow rate data of Mazzini et al. (2007). Substituting the assumed values to Equations (1)–(3) gives the maximum LOS displacement of 29.0 cm for $R \geq 1 \text{ km}$ (note that our interferograms do not measure the displacements on the closer mud-covered area). Although our estimation is based on a simplified model, the assumed parameter values are conservative and hence it is probably difficult to explain the observed several tens of centimeters of range increase solely by the loading effect. Moreover, the interferograms show that the range increase signals around the mud-flooded area are not perfectly correlated with the distance from the flooded area, and the range decrease signals to the east (zone B in Fig. 4) cannot be produced by loading. These facts further suggest that loading is not the dominant subsidence mechanism.

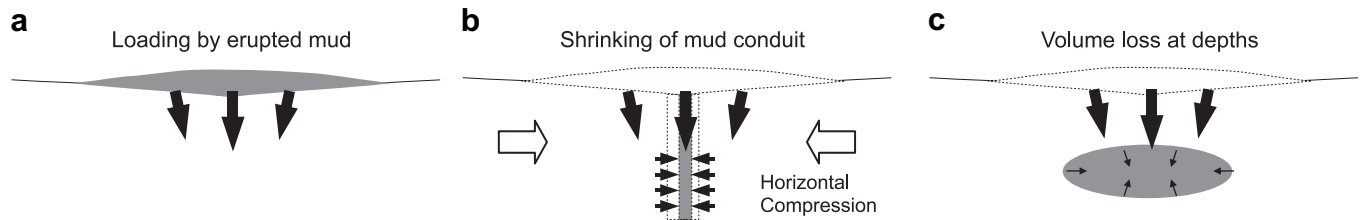


Fig. 5. Schematic figures showing possible driving sources of subsidence.

A cylindrical conduit is developed as the material of the mud pathway is being eroded. The conduit is filled with mud having its own pressure. If the horizontal tectonic stress is in compression and is greater than the pressure of mud in the conduit, then the surrounding medium experiences inward displacements and subsidence (Fig. 5(b)). Displacements U_{cylinder} at the surface $z=0$ caused by a finite line source representing a pressured vertical cylindrical conduit can be described by (Walsh and Decker, 1971; Voight et al., 1999)

$$U_{\text{cylinder}} = 2a^2 \frac{\Delta P}{E} (1 - \sigma^2) \left\{ \frac{1}{r} \left[\frac{c_2}{R_2} - \frac{c_1}{R_1} \right] \hat{r} + \left[\frac{1}{R_2} - \frac{1}{R_1} \right] \hat{z} \right\}, \quad (4)$$

where a is the radius of the conduit, ΔP is the pressure change within the conduit, c_1 and c_2 are the depths from the surface to the top ($z=c_1$, $r=0$) and bottom of the line source ($z=c_2$, $r=0$), $R_i = (r^2 + c_i^2)^{1/2}$ are the distances from any point at the surface to the top and bottom of the line source, \hat{r} and \hat{z} are the unit vectors in the r and z coordinate directions.

Here we assume that the horizontal stress is equal to the lithostatic pressure with rock density 2100 kg/m^3 . This assumption is reasonable for the considered mechanically-weak sediment layer. The mud pressure is assumed to be hydrostatic with density 1440 kg/m^3 . These assumptions lead to an overpressure gradient of 6.5 kPa/m , resulting in 0 MPa at the surface and 18 MPa at 2800 m . The conduit considered in Equation (4) is discretized and the solutions are numerically integrated to calculate the displacements due to the linearly-varying pressure change. Substituting other values of $a = 25 \text{ m}$, $c_1 = 0 \text{ m}$, $c_2 = 2800 \text{ m}$, $E = 0.1 \text{ GPa}$, and $\sigma = 0.25$ leads to a maximum LOS displacement of 7.7 cm 1 km away from the surface location of the conduit. Note that our estimate gives the upper bound of the possible displacements, because, in reality, the pressure change gradient is probably smaller or may even have an opposite sign with the presence of the overpressure of the mud source. The effect of the formation of such a conduit can therefore be neglected, as long as the size of the conduit is on the order of the presumed value. It should be noted, however, that a greater conduit in radius would cause the same type of deformation but with larger amplitudes, as the displacements are scaled by the square of the radius of the cylinder (Equation (4)).

Lastly and most significantly, release of pore overpressure and depletion of material at depth can cause observed ground deformation (Fig. 5(c)), in the same manner as commonly observed ground subsidence due to water withdrawal from pumping and deflation of magma reservoirs on volcanoes. This effect is further investigated with a boundary-element modeling in the next subsection.

3.2. Boundary-element modeling

Ellipsoidal fringes observed in the interferograms A1 (19 May–4 Oct. 2006) and A2 (4 Oct.–19 Nov. 2006) exhibit relatively simple displacements (see Fig. 3), which allows us to assume a simple single source to explain the displacements. Here, an inversion

method that combines a mixed boundary element method (BEM) with a Monte-Carlo inversion method (Fukushima et al., 2005) is used to obtain models that quantitatively explain the first two interferograms. The rest of the interferograms have less coherent signals and are not modeled in this study. The mixed BEM (Cayol and Cornet, 1997) can perform, using triangular mesh elements, 3D model computations under assumptions of linear elasticity, homogeneity and isotropy, with realistic topography taken into account. The mixed BEM has been applied to volcanic deformation problems (e.g. Cayol and Cornet, 1998; Beauducel and Cornet, 1999). As the inversion algorithm, a neighborhood algorithm (Sambridge, 1999a) is used. The combined method has previously been applied to problems related to magma transfer on volcanoes (Froger et al., 2004; Fukushima, 2005; Fukushima et al., 2005; Peltier et al., 2008).

Preliminary inversions indicated that the range decrease east of the subsidence area (zone B in Fig. 4) could not be well explained by a horizontal penny-shaped crack model; an oblate spheroid is hence assumed instead. Since the longer and shorter axes of the ellipsoidal displacement pattern are approximately oriented north–south and east–west, the longest axis is fixed to north–south, intermediate axis to east–west, and shortest axis to vertical. For simplicity, a constant negative pressure change is assumed. Computationally, the oblate spheroid deflates in response to this negative pressure change. In the boundary-element computations, Young's modulus of 0.1 GPa and Poisson's ratio of 0.25 are assumed. Because the ground displacements are proportional to the pressure change and inversely proportional to Young's modulus, the assumed Young's modulus only affects the estimation of the pressure change and not the other parameters or the volume change estimation. Seven model parameters, i.e., the horizontal coordinates of the center, top depth, lengths of the three axes, pressure change, are estimated by the inversion method.

A topography mesh, having 1822 elements in a circular area of radius 8 km , is created using the SRTM DEM and this mesh is commonly used for all the forward model computations of the BEM. Although the computations take into account the topography, the target region is nearly flat, and thus the topography has practically no effect on the results. The mesh of the oblate spheroid is automatically generated before every BEM computation during an inversion run. Irrespective of the geometry, the number of elements of the mesh of the spheroid is fixed to 320. The precision of the BEM computation depends on the mesh densities and the spatial extension of the topography mesh; the meshes we use have the densities and spatial extension (for topography) that have been confirmed to be precise enough for our purpose (Fukushima, 2005). The displacements (and stresses) at the center of every elements are computed by the BEM; the displacements are interpolated on the data points used in the misfit evaluation step of the inversions.

Before inversions, the interferograms are transformed into local kilometer coordinates with the center of the mud-covered area set as the origin, then phase-unwrapped (conversion from phase to LOS displacements) and subsampled in concentric grids (Fig. 6). The subsampling is done in such a way that the density of the data

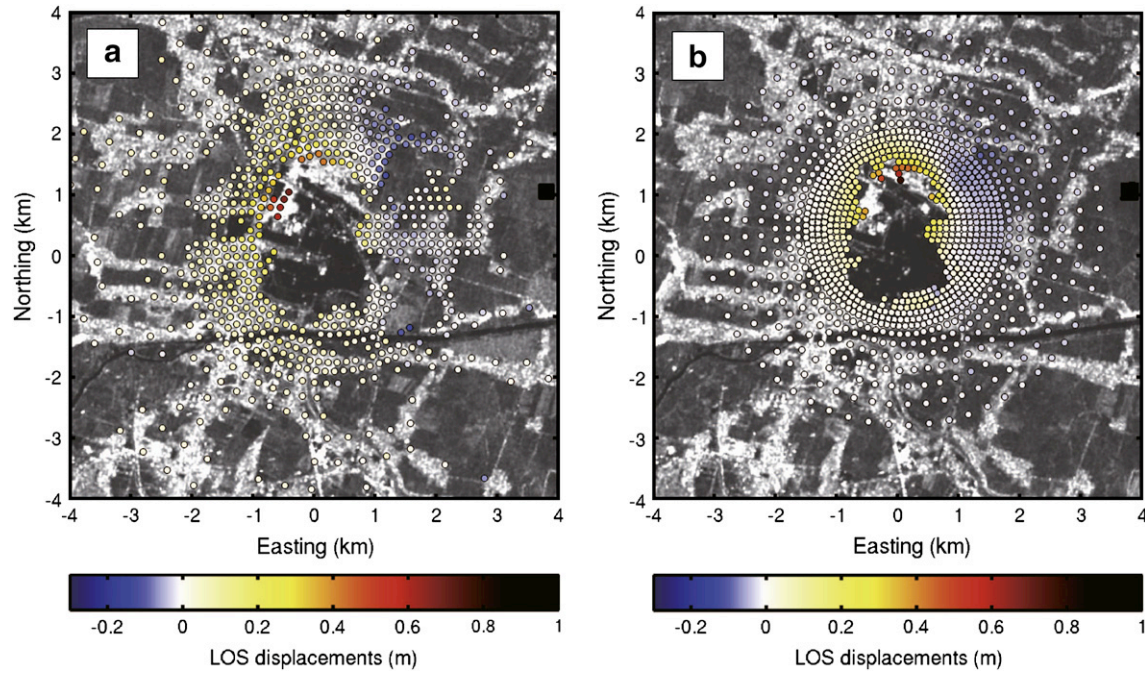


Fig. 6. (a) Data used for inversion subsampled from the unwrapped interferogram of A1, superimposed on a SAR intensity image. Color indicates the LOS displacements (positive away from the satellite). (b) Same for interferogram A2 (For interpretation of the references to color in this figure legend, the reader is referred to the web version of this article.).

points becomes small far from the deformation center. This concentric subsampling method has been shown not to bias the model results for a similar problem (Fukushima et al., 2005). Areas where no meaningful signal is obtained (e.g. mud-covered areas) are masked before unwrapping and not used in the inversion. The numbers of subsampled points are 789 and 1047 for the interferograms A1 and A2, respectively.

The neighborhood algorithm we use works as follows. First, n initial models are randomly chosen and evaluated. Next, at each iteration, n new points are generated in the neighborhood (in the model space) of the n lowest misfit models. The “neighborhood” is defined by Voronoi cells. Iterations continue until the misfit converges. We use $n = 30$ in this study, which has been found to be a good compromise between the speed of convergence and extensivity of the search in similar past studies (Fukushima et al., 2005). Multiple runs on the same inversion problem with $n = 30$ lead to effectively the same result, suggesting that the obtained solutions found the global minimum.

We use a misfit function defined as

$$\chi^2(\mathbf{m}) = (\mathbf{u}_0 - \mathbf{u}_m)^T \mathbf{C}_d^{-1} (\mathbf{u}_0 - \mathbf{u}_m), \quad (5)$$

where $\mathbf{u}_0 = [u_0^1, u_0^2, \dots, u_0^N]$ and $\mathbf{u}_m = [u_m^1, u_m^2, \dots, u_m^N]$ represent observed and modeled displacement vectors, respectively, and \mathbf{C}_d is the data covariance matrix. The modeled displacement u_m^i for the i -th data point is calculated from the three dimensional displacement (u_x^i, u_y^i, u_z^i) by

$$u_m^i = -\left(u_x^i, u_y^i, u_z^i\right) \begin{pmatrix} s_1^i & s_2^i & s_3^i \end{pmatrix}^T, \quad (6)$$

where (s_1^i, s_2^i, s_3^i) is a LOS unit vector computed from satellite orbit data for i -th data point. Phase-unwrapped interferograms contain an unknown offset because the resulting displacement values are not referenced. This unknown constant is automatically determined for each misfit evaluation in such a way that the misfit becomes minimum, and the offset is subtracted from the unwrapped data to obtain \mathbf{u}_0 .

Interferometric data contain spatially-correlated random noise due to atmospheric phase delays and also spatially-correlated model error. A full data covariance matrix \mathbf{C}_d is assumed here with an exponential correlation model

$$C(r) = \epsilon^2 \exp(-r/a), \quad (7)$$

where r denotes the distance between two data points. The correlation length a is set to 300 m based on autocorrelation analysis of the residual data of several inversion runs. The variance ϵ^2 does not change the results of search problems and hence a unit value is assumed. A previous study has shown (Fukushima et al., 2005) that the results do not significantly differ by different subsampling methods when a full data covariance matrix is assumed.

Once an inversion search run is finished, the confidence intervals of the model parameters are determined from direct evaluation of the marginal probability density function of the model parameters (Sambridge, 1999b; Fukushima et al., 2005). Since the variance ϵ^2 in Equation (7) affects the model uncertainty analysis, the misfit values evaluated during the model search stage are multiplied by the variance of residual data before determination of the confidence intervals (Fukushima et al., 2005).

The inversion results are listed in Table 2. For an inversion of the interferogram A1 (19 May–4 Oct. 2006), the ellipsoidal fringe pattern as well as the range decrease area to the east, are explained by the optimum model (Fig. 7). The center of the spheroid is located beneath the main eruptive vent. Unexplained signals can mainly be attributed to our assumptions of the simplified geometry and constant pressure change of the source of deformation, as well as the assumed Poisson's ratio.

An inversion on the interferogram of the subsequent 46 days (4 Oct.–19 Nov. 2006) produced a model having a larger pressure change and a smaller source size (Fig. 8). The center of the spheroid is shifted about 200 m to the north, explaining the signals close to the northern rim of the mud-covered area rather than the smaller signals observed close to the southern rim (red arrow in Fig. 8(a)). The northward shift of the deformation source is significant

Table 2

Inversion results of an oblate spheroid model. Subscripts and superscripts are the lower and upper bounds of the 95% confidence intervals.

Data ^a	Pressure change (MPa)	Center coordinate (X,Y), (m)	Top depth (m)	Bottom depth (m)	NS axis (m)	EW axis (m)	Data explained (%) ^b
A1	$-0.14_{-0.23}^{+0.11}$	$(202.7_{147.6}^{228.2}, 767.5_{692.8}^{811.0})$	$420.4_{346.0}^{592.0}$	$934.2_{1565.7}^{1277.1}$	$2061.2_{1565.7}^{2261.2}$	$1049.8_{915.9}^{1499.1}$	89.3
A2	$-0.39_{-0.42}^{+0.27}$	$(227.7_{187.6}^{259.5}, 946.6_{882.0}^{1006.2})$	$467.5_{426.0}^{544.9}$	$682.7_{584.4}^{765.0}$	$1046.2_{1026.9}^{1177.6}$	$769.6_{665.2}^{796.0}$	90.9
A1	$-0.79_{-0.80}^{+0.52}$	$(172.6_{100.6}^{233.9}, 838.1_{740.2}^{920.3})$	1200 ^c	$1244.5_{1220.5}^{1338.6}$	$1514.6_{1181.2}^{1821.3}$	$742.2_{387.3}^{1282.6}$	80.5

^a See Table 1 for the dates.^b Computed in a least square's sense. Values cannot be directly compared for inversions performed on different datasets.^c Fixed value.

considering the confidence intervals of approximately ± 60 m (Table 2). The phase change on the southern rim is discontinuous, which is consistent with a few centimeters of collapse bounded by a fault reaching or nearly reaching the ground.

The top depths of the two estimated models are comparable, but the bottom depth of the model for the 4 Oct.–19 Nov. 2006 period is 360 m shallower (Table 2). This appears to be reasonable considering the smaller spatial extension of the deformed area. Considering that the deformed areas in the interferograms spanning later time periods (A3–A5, D1–D3 in Fig. 3) are similar to those of A2 (4 Oct.–19 Nov. 2006), the source of deformation should be shallow for the later periods as well. Mazzini et al. (2007) compared their clay mineral analyses on collected mud samples to the borehole biostratigraphy data and showed that the erupting mud has a deep origin and is migrating from depths of at least 1219 m and probably as deep as 1828 m. The depths of the source of deformation determined from the inversions are significantly shallower than their estimation.

4. Discussion

4.1. Depth of the deformation source

To further consider the depth issue, a supplementary inversion was performed to check if a deep source could also explain the signals by fixing the top depth to 1200 m. The displacements produced by this model do not fit the observation very well, with the percentage of explained data 80.5%, compared to 89.3% for the shallower model (Table 2). The modeled interferogram has broader fringes with larger residual amplitudes on the northern half around the mud-covered area (Fig. 9).

The well log data of Banjarpanji-1 and nearby Wunut-4 suggest Young's moduli of approximately 1 GPa and 60 GPa shallower and deeper than 1800 m, respectively (Lapindo, unpublished data). The upper layer consists of clays, sands and shales, whereas the lower layer principally contains compact volcanoclastic sands (Mazzini et al., 2007; Davies et al., 2008; Istadi et al., submitted for publication). We made a model calculation with a propagator matrix method to check how such a layered structure affects our depth estimation. Since the mixed BEM cannot take into account layered structures in the current implementation, we used solutions for a point source. We consider a two-layer model having 0.1 GPa down to 1.8 km and 30 GPa for deeper depths (Fig. 10(a)). Here we assumed a static/dynamic ratio of 0.1 for the upper porous layer and 0.5 for the lower more compact layer. The layered model is compared with a homogeneous model having a constant Young's modulus of 0.1 GPa (Fig. 10(b)).

Fig. 11 shows the ground displacements computed for a point deflating source located at 600 m depth, which roughly corresponds to the depth center of our estimated spheroids, both for the layered and homogeneous models. The layered model predicts displacements more localized near the source. To check how much this difference influences inversion results, horizontal and vertical displacements calculated for the two-layer model (as in Fig. 11) were inverted with the half-space assumption. When the source was shallow (far from the layer boundary), the half-space assumption only slightly underestimated the depth (Fig. 12). For example, when the “true source” was at 600 m, then the depth inverted with the half-space assumption was 576 m, which corresponds to only a 4.0% of difference. This insensitivity to the layered structure is consistent with the result of a similar test obtained from finite element computations (Masterlark, 2007, see his

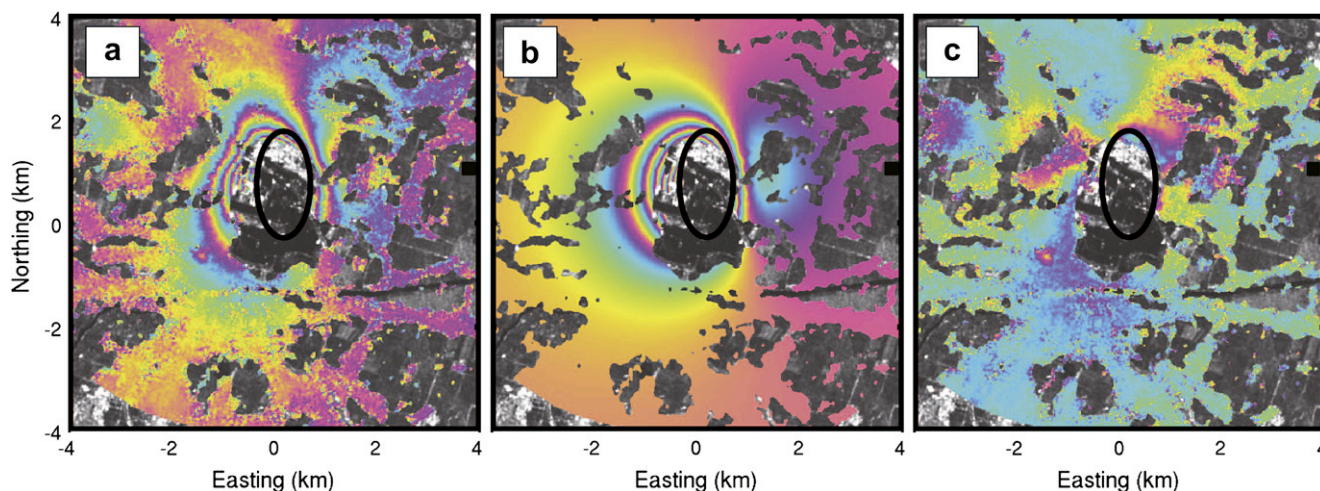


Fig. 7. (a) Interferogram A1 spanning 19 May and 4 Oct. 2006, superimposed on a SAR intensity image. Areas unused by the inversion are masked. Refer to the caption of Fig. 2 for the meaning of the colors. Black ellipsoid shows the location of the optimum oblate spheroid determined by the inversion. (b) Modeled interferogram corresponding to the optimum model. (c) Residual interferogram containing unexplained signals.

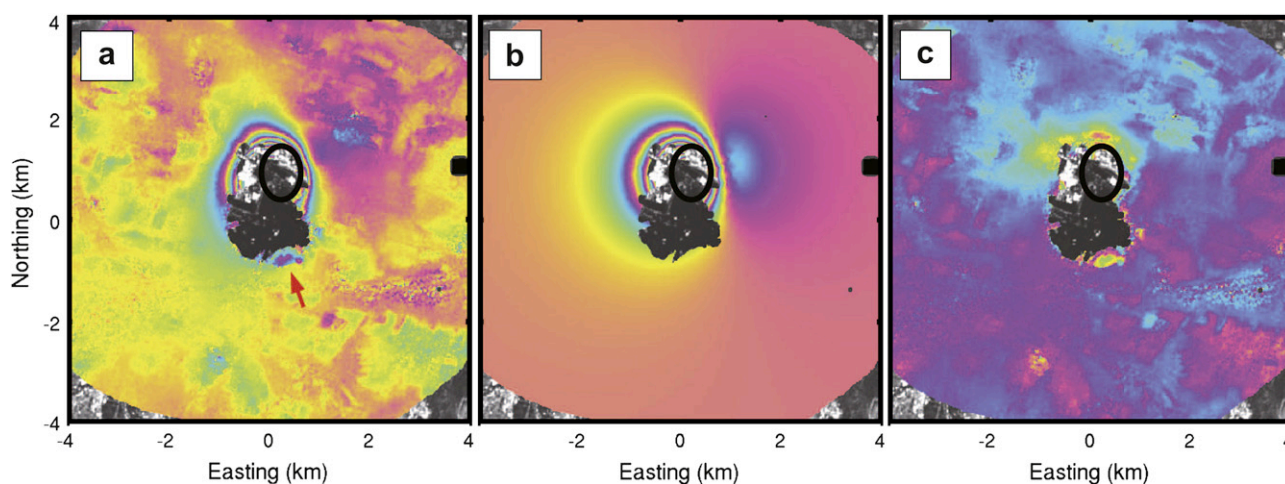


Fig. 8. (a) Interferogram A2 spanning 4 Oct. and 19 Nov. 2006, superimposed on a SAR intensity image. Areas unused by the inversion are masked. Refer to the caption of Fig. 2 for the meaning of the color. Black ellipsoid shows the location of the optimum oblate spheroid determined by the inversion. Red arrow indicates discontinuous displacements that may be attributed to a subsidence bounded by a fault. (b) Modeled interferogram corresponding to the optimum model. (c) Residual interferogram (For interpretation of the references to color in this figure legend, the reader is referred to the web version of this article.).

Figure 11a). The percentage of underestimation exceeded 10% for the “true” depth greater than 1250 m. Even if we have underestimated the depths by 10% in our modeling, our depth ranges (top to bottom depths, see Table 2) do not practically overlap the depths constrained by the mud samples.

From the above discussion, we conclude that the extended source that caused the surface deformation should lie at depths shallower than the erupting mud.

4.2. Volume changes

The volume changes for the optimum models were $2.8 \times 10^6 \text{ m}^3$ (19 May–4 Oct. 2006) and $1.5 \times 10^6 \text{ m}^3$ (4 Oct.–19 Nov. 2006). The semi-quantitative eruption volume estimates (Mazzini et al., 2007) give values of $8.0 \times 10^6 \text{ m}^3$ and $1.0 \times 10^6 \text{ m}^3$ for the corresponding periods, respectively. The erupted volume is larger than the deflated volume in the first four months, and is of the same order for the next 46 day. This may indicate that a rapid pressure decrease in a high eruption rate stage was compensated by time-dependent

deformation in the subsequent relatively quiet period. Alternatively, the volume difference in the first four months can be explained by the compressibility of mud (Rivalta and Segall, 2008); the mud could be highly compressed with high pressure in the initial stage.

4.3. Conceptual model

To both explain our results and the analysis of the mud samples (Mazzini et al., 2007), the source of the surface deformation may be spread over a shallower depth range than the source of the eruptive products. One possible explanation of this depth difference is that there could be inelastic deformation, including compaction, downward material transfer and subsurface faulting, occurring in association with the eruption (Fig. 13). Such a process concentrates deformation in regions above the source of eruptive products. In effect, caldera formation and associated normal faulting are commonly observed on mud volcanoes (e.g. Planke et al., 2003; Stewart and Davies, 2006).

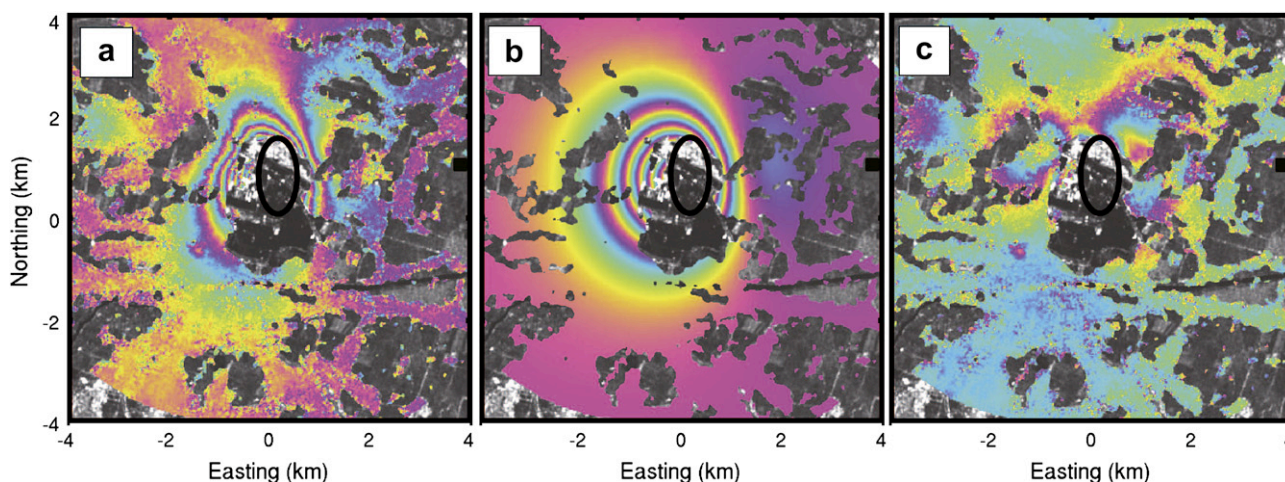


Fig. 9. Inversion result obtained with the top depth of the oblate spheroid fixed at 1200 m. (a) Same as Fig. 7(a), except the location of the optimum source. (b) Modeled interferogram corresponding to the optimum model. (c) Residual interferogram.

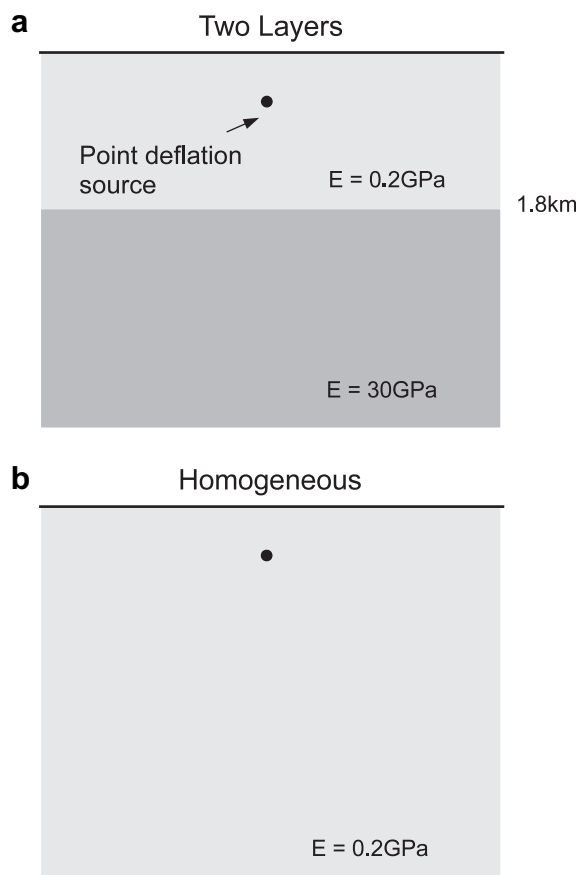


Fig. 10. Setting of the compared two models. (a) Two-layer model having Young's moduli 0.1 GPa from the surface to 1800 m and 30 GPa below. (b) Homogeneous model having a constant Young's modulus of 0.1 GPa.

Displaced rail tracks observed west of the crater in the first months (Media Center LUSI, 2006) and the discontinuity in LOS displacements in the interferogram A2 (red arrow in Fig. 8(a)) support the presence of partial subsurface faulting. Our proposed model is similar to what has been believed as the cause of ground subsidence due to pumping in populated areas (Holzer and Johnson, 1985) as well as in geothermal and oil fields (e.g. Bondor and de Rouffignac, 1995). The results of the two inversions, one on the data of the first four months and the other on the subsequent 46 days, indicated shallowing of the deformation source. This is again consistent with our conceptual model (Fig. 13), because at an early stage, the pressure decrease associated with the depletion of material could occur at deeper depths.

4.4. Future work

The interferograms after 19 Nov. 2006 appear to be similar, indicating a stable situation. Does this guarantee that no catastrophic collapse will occur in the future? To answer this question, we still need further investigation. The most important issue to consider is the stress state of LUSI. If the system evolves in such a way that the mechanical equilibrium is attained by continuous subsidence and recharge, then there is no risk of a sudden large collapse. Several kinds of geophysical surveys including gravity and GPS have been conducted (Istadi et al., submitted for publication), which can provide complementary data in order to investigate this problem. Based on the evaluation of several subsidence mechanisms (Section 3.1), the smaller amount of displacements observed after January 2007 could be explained by the loading of the erupted mud and

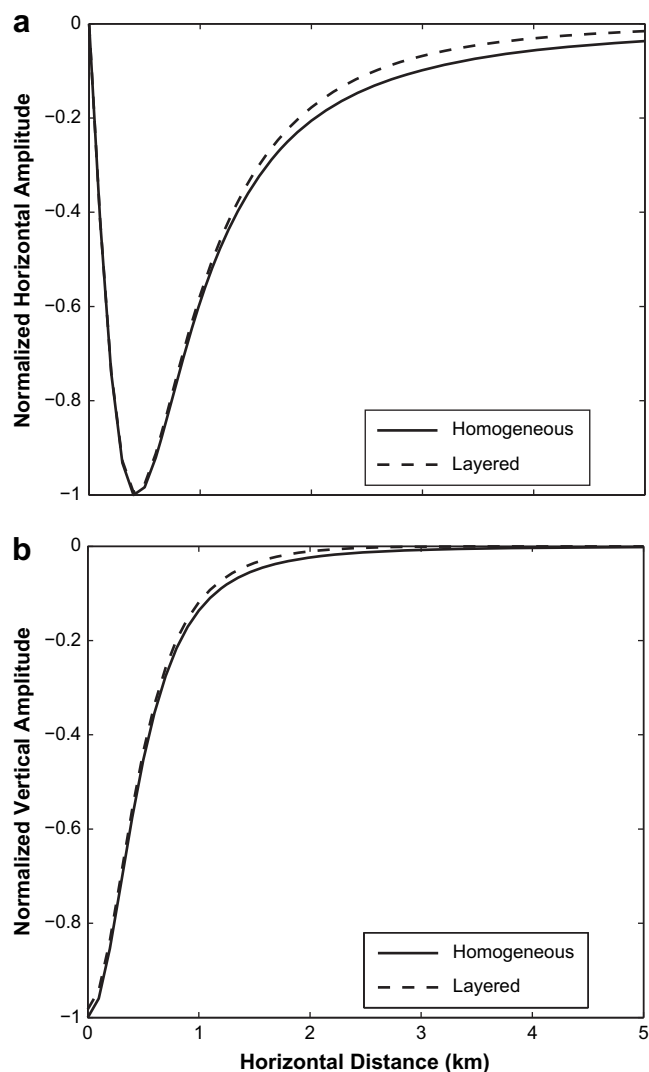


Fig. 11. (a) Horizontal and (b) vertical displacements predicted for a point deflation source at 600 m in the two-layer and homogeneous models described in Fig. 10. The amplitudes are normalized by the maximum absolute values of the homogeneous solution.

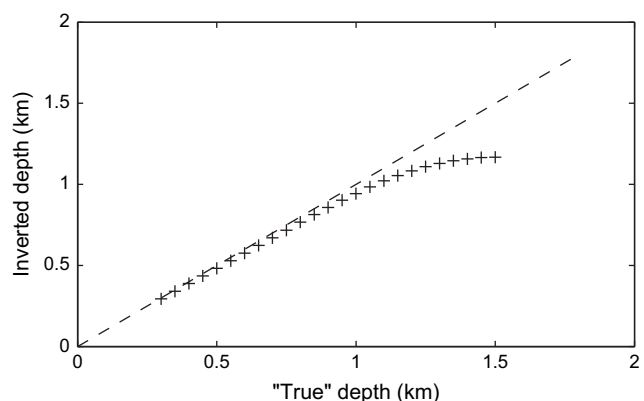


Fig. 12. Depths inverted with the half-space assumption from the horizontal and vertical displacements calculated for the two-layer model shown in Fig. 10 (plus signs). Data below the broken line indicate that the depth was determined shallower than the assumed value (underestimation).

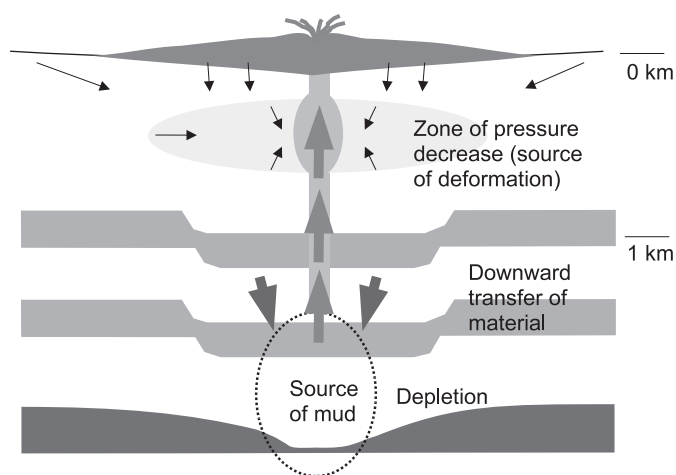


Fig. 13. Conceptual model that explains our modeling results and the depth of the erupted material determined by Mazzini et al. (2007). Depletion of material deeper than 1200 m is accompanied by compaction, downward transfer of upper material, and possibly normal fault formation. These processes decrease the effective pressure at shallower depths of several hundred meters, which is detected as the source of the ground surface subsidence.

expansion of the conduit size. The effects of these two subsidence mechanisms should also be investigated in further studies.

5. Conclusions

The processed SAR interferograms covering a time period of one year from the onset of the LUSI mud eruption in May 2006 persistently showed subsidence over an ellipsoidal area of approximately 4 km × 3 km centered on the main eruptive vent. Effects of loading of mud and creation of a cylindrical mud conduit of a radius of a few tens of meters are too small to explain the total amount of ground subsidence observed in the first six months of the eruption. Depletion of material and decrease of fluid pressure at depth are thus probably the dominant cause of the subsidence. We found that deflation of an oblate spheroid lying shallower than 1 km explains the observed displacements. Considering the difference of the depths of the source of deformation and of the erupted mud estimated by Mazzini et al. (2007) (1.2–1.9 km), we suggest a conceptual model of subsidence where compaction and downward material transfer fill the space depleted by the eruptive products from deeper levels. SAR interferometry using PALSAR products and mechanical modeling can continue to contribute to map the ground subsidence and infer the ongoing subsurface processes; for assessing future risks in more detail, a joint analysis with GPS and gravity data would be valuable.

Acknowledgements

Part of the PALSAR data used in this study is shared by PIXEL (PALSAR Interferometry Consortium to Study our Evolving Land surface) and is provided from the Japan Aerospace Exploration Agency (JAXA) through a joint research contract between JAXA and the Earthquake Research Institute, University of Tokyo. The ownership of PALSAR data belongs to JAXA and Ministry of Economy, Trade and Industry of Japan. This research is conducted partly as a joint research project of the Earthquake Research Institute, University of Tokyo. The authors are grateful to Adriano Mazzini and Bambang Istadi for discussions, Sunu Praptono of Lapindo for the well log data, and Kaj Johnson for his code of layered half-space model calculation. Comments from an anonymous reviewer and Mike Poland significantly improved the paper.

This work was partially supported by the Grant-in-Aid for Scientific Research from the Ministry of Education, Culture, Sports, Science and Technology (No.20403007).

References

- Abidin, H.Z., Davies, R.J., Kusuma, M.A., Andreas, H., Deguchi, T., 2008. Subsidence and uplift of Sidoarjo (East Java) due to the eruption of the Lusi mud volcano (2006–present). *Environmental Geology* doi:10.1007/s00254-008-1363-4.
- Amelung, F., Galloway, D.L., Bell, J.W., Zebker, H.A., Lacznak, R.J., 1999. Sensing the ups and downs of Las Vegas: InSAR reveals structural control of land subsidence and aquifer-system deformation. *Geology* 27 (6), 483–486.
- Berry, P.A.M., Garlick, J.D., Smith, R.G., 2007. Near-global validation of the SRTM DEM using satellite radar altimetry. *Remote Sensing of Environment* 106 (1), 17–27.
- Beauducel, F., Cornet, F.H., 1999. Collection and three-dimensional modeling of GPS and tilt data at Merapi volcano, Java. *Journal of Geophysical Research* 104, 725–736.
- Bondor, P.L., de Rouffignac, E., 1995. Land subsidence and well failure in the Belridge diatomite oil field, Kern county, California. Part II. Applications. In: Barends, F.B.J., Brouwer, F.J.J., Schröder, F.H. (Eds.), *Land Subsidence*. IAHS Press, Wallingford, Oxfordshire, UK, pp. 69–78.
- Carnec, C., Delacourt, C., 2000. Three years of mining subsidence monitored by SAR interferometry, near Gardanne, France. *Journal of Applied Geophysics* 43 (1), 43–54.
- Cayol, V., Cornet, F.H., 1997. 3D mixed boundary elements for elastostatic deformation fields analysis. *International Journal of Rock Mechanics and Mining Sciences Abstract* 34, 275–287.
- Cayol, V., Cornet, F.H., 1998. Three-dimensional modeling of the 1983–1984 eruption at Piton de la Fournaise Volcano, Reunion Island. *Journal of Geophysical Research* 103, 18025–18037.
- Cheng, C.H., Johnston, D.H., 1981. Dynamic and static moduli. *Geophysical Research Letters* 8, 39–42.
- Davies, R.J., Swarbrick, R.E., Evans, R.J., Huuse, M., 2007. Birth of a mud volcano: East Java, 29 May 2006. *GSA Today* 17 (2), 4–9.
- Davies, R.J., Brumm, M., Manga, M., Rubiandini, R., Swarbrick, R., Tingay, M., 2008. The East Java mud volcano (2006 to present): an earthquake or drilling trigger? *Earth and Planetary Science Letters* 272, 627–638.
- Deguchi, T., Kato, M., Akcin, H., Kutoglu, H.S., 2007a. Monitoring of mining induced land subsidence using L- and C-band SAR interferometry. In: *Geoscience and Remote Sensing Symposium, IGARSS 2007, IEEE International*, pp. 2122–2125.
- Deguchi, T., Maruyama, Y., Kato, M., 2007b. Measurement of long-term deformation by InSAR using ALOS/PALSAR data. In: *Presented at FRINGE 2007 workshop, November 2007, Frascati, Italy*. Workshop presentation available from: <http://earth.esa.int/cgi-bin/conf/fringe07.pl?abstract=186> Workshop proceedings are in press.
- Farr, T.G., Kobrick, M., 2000. Shuttle radar topography mission produces a wealth of data. *Eos Transactions, American Geophysical Union* 81 (48), 583–585.
- Fielding, E.J., Blom, R.G., Goldstein, R.M., 1998. Rapid subsidence over oil fields measured by SAR interferometry. *Geophysical Research Letters* 25 (17), 3215–3218.
- Froger, J.-L., Fukushima, Y., Briole, P., Staudacher, T., Souriot, T., Villeneuve, N., 2004. The deformation field of the August 2003 eruption at Piton de la Fournaise, Reunion Island, mapped by ASAR interferometry. *Geophysical Research Letters* 31 L14601. doi:10.1029/2004GL020479.
- Fukushima, Y., 2005. Magma Transfer at Piton de la Fournaise Volcano from 3D Modelling of Radar Interferometric Data for 1998–2000. Ph.D. thesis, Université Blaise Pascal. Available from: <http://tel.ccsd.cnrs.fr/tel-00011582>.
- Fukushima, Y., Cayol, V., Durand, P., 2005. Finding realistic dike models from interferometric synthetic aperture radar data: the February 2000 eruption at Piton de la Fournaise. *Journal of Geophysical Research* 110 B03206. doi:10.1029/2004JB003268.
- Goldstein, R.M., Werner, C.L., 1998. Radar interferogram filtering for geophysical applications. *Geophysical Research Letters* 25 (21), 4035–4038.
- Gourmelen, N., Amelung, F., Casu, F., Manzo, M., Lanari, R., 2007. Mining-related ground deformation in Crescent Valley, Nevada: implications for sparse GPS networks. *Geophysical Research Letters* 34 L09309. doi:10.1029/2007GL029427.
- Hanssen, R.F., 2001. *Radar Interferometry – Data Interpretation and Error Analysis*. Kluwer Academic Publishers, Dordrecht, The Netherlands.
- Holzer, T.L., Johnson, A.L., 1985. Land subsidence caused by ground water withdrawal in urban areas. *Geojournal* 11 (3), 245–255.
- Istadi, B.P., Pramono, G.H., Sumintadireja, P., Alam, S., 2009. Modeling study of growth and potential geohazard for LUSI mud volcano: East Java, Indonesia. *Journal of Marine and Petroleum Geology* 26, 1724–1739.
- Jaeger, J.C., Cook, N.G.W., Zimmerman, R.W., 2007. *Fundamentals of Rock Mechanics*, fourth ed. Blackwell Publishing, Malden.
- Manga, M., 2007. Did an earthquake trigger the May 2006 eruption of the Lusi mud volcano? *Eos Transactions, American Geophysical Union* 88, 201.
- Massonnet, D., Holzer, T., Vadon, H., 1997. Land subsidence caused by the East Mesa geothermal field, California, observed using SAR interferometry. *Geophysical Research Letters* 24 (8), 901–904.

- Massonnet, D., Feigl, K.L., 1998. Radar interferometry and its application to changes in the Earth's surface. *Review of Geophysics* 36, 441–500.
- Masterlark, T., 2007. Magma intrusion and deformation predictions: sensitivities to the Mogi assumptions. *Journal of Geophysical Research* 112 B06419. doi:10.1029/2006JB004860.
- Mazzini, A., Svensen, H., Akhmanov, G.G., Aloisi, G., Planke, S., Malthe-Sørenssen, A., Istadi, B., 2007. Triggering and dynamic evolution of the LUSI mud volcano, Indonesia. *Earth and Planetary Science Letters* 261, 375–388.
- Media Center LUSI, November 2006. Newspaper published by Timnas Penanggulangan Semburan Lumpur di Sidoarjo, fifth ed., (in Indonesian).
- Peltier, A., Famin, V., Bachèlery, P., Cayol, V., Fukushima, Y., Staudacher, T., 2008. Cyclic magma storages and transfers at Piton de La Fournaise volcano (La Réunion hotspot) inferred from deformation and geochemical data. *Earth and Planetary Science Letters* 270, 180–188. doi:10.1016/j.epsl.2008.02.042.
- Planke, S., Svensen, H., Hovland, M., Banks, D.A., Jamtveit, B., 2003. Mud and fluid migration in active mud volcanoes in Azerbaijan. *Geo-Marine Letters* 23, 258–268.
- Rivalta, E., Segall, P., 2008. Magma compressibility and the missing source for some dike intrusions. *Geophysical Research Letters* 35 L04306. doi:10.1029/2007GL032521.
- Rosen, P.A., Hensley, S., Zebker, H.A., Webb, F.H., Fielding, E.J., 1996. Surface deformation and coherence measurements of Kilauea Volcano, Hawaii, from SIR C radar interferometry. *Journal of Geophysical Research* 101 (E10), 23109–23126.
- Sambridge, M., 1999a. Geophysical inversion with a neighbourhood algorithm – I. Searching a parameter space. *Geophysical Journal International* 138, 479–494.
- Sambridge, M., 1999b. Geophysical inversion with a neighbourhood algorithm – II. Appraising the ensemble. *Geophysical Journal International* 138, 727–746.
- Stewart, S.A., Davies, R.J., 2006. Structure and emplacement of mud volcano systems in the South Caspian Basin. *AAPG Bulletin* 90, 753–770.
- van Heerden, W.L., 1987. General relations between static and dynamic moduli of rocks. *International Journal of Rock Mechanics and Mining Sciences Abstract* 24, 381–385.
- van Noorden, R., 2006. Java mud volcano seems unstoppable. *Nature News* doi:10.1038/news060925-13.
- Voight, B., et al., 1999. Magma flow instability and cyclic activity at Soufriere Hills volcano, Montserrat, British West Indies. *Nature* 283, 1138–1142.
- Walsh, J., Decker, R., 1971. Surface deformation associated with volcanism. *Journal of Geophysical Research* 76 (14), 3291–3302.
- Zebker, H.A., Villasenor, J., 1992. Decorrelation in interferometric radar echoes. *IEEE Geoscience and Remote Sensing Letters* 30, 950–959.